Journal of Membrane Science 617 (2021) 118640

Contents lists available at ScienceDirect

Journal of Membrane Science

journal homepage: http://www.elsevier.com/locate/memsci

Controlling molten carbonate distribution in dual-phase molten salt-ceramic membranes to increase carbon dioxide permeation rates

Maria Kazakli [a], Greg A. Mutch [a], Georgios Triantafyllou [a], Ana Gouveia Gil [a], Tao Li [b], Bo Wang [b], Josh J. Bailey [c,d], Dan J.L. Brett [c,d], Paul R. Shearing [c,d], Kang Li [b], Ian Metcalfe [a,*]

[a] Materials, Concepts and Reaction Engineering (MatCoRE) Group, School of Engineering, Newcastle University, Newcastle Upon Tyne, NE1 7RU, UK
[b] Barrer Centre, Department of Chemical Engineering, Imperial College London, London, SW7 2AZ, UK
[c] Electrochemical Innovation Lab, Department of Chemical Engineering, University College London, London, WC1E 7JE, UK
[d] The Faraday Institution, Quad One, Becquerel Ave, Harwell Campus, Didcot, OX11 0RA, UK

ARTICLE INFO

Keywords:
Carbon dioxide separation
Dual-phase molten salt-ceramic membrane
Hollow-fibre membrane
Molten carbonate

ABSTRACT

Dual-phase molten salt-ceramic membranes show high permselectivity for CO_2 when molten carbonate is supported in a porous oxygen-ion and/or electron conductor. In this arrangement, the support likely contributes to permeation. Thus, if one is to understand and ultimately design membranes, it is also important to perform experiments with an inert support where permeation relies upon the molten carbonate properties alone. Here, a nominally inert material (Al_2O_3) was used in order to restrict permeation to molten carbonate. Model Al_2O_3 dual-phase membranes were fabricated using laser drilling to provide an order of magnitude difference in molten salt-gas interfacial area between feed and permeate sides. Molten carbonate thickness in the model membranes was also varied, independent of the molten salt-gas interfacial area. For all thicknesses studied, CO_2 permeation rates showed a significant temperature dependence from 500 to 750 °C, suggesting an activated process was rate-limiting, likely a permeate-side molten salt-gas interfacial process, *i.e.* desorption of CO_2. We applied these findings in asymmetric hollow-fibre supports, a geometry with inherent modularity and scalability, by developing a new carbonate infiltration method to control molten carbonate distribution within the hollow fibre. Compared to a conventionally prepared dual-phase hollow-fibre membrane with an uncontrolled distribution of carbonates, permeation rates were increased by up to 4 times when the molten salt was confined to the packed-pore network, *i.e.* without infiltrating the hollow-fibre micro-channels. X-ray micro-CT investigations supported the idea that the resulting increase in interfacial area for desorption of CO_2 was the key structural difference contributing to increased permeation rates. For CO_2 separation, where large volumes of gas must be processed, such increases in permeation rates will reduce the demand for membrane materials, although one must note the higher permeation rates achievable with oxygen-ion and/or electron conducting supports.

1. Introduction

Highly permselective separation of CO_2 has been realised by dual-phase molten salt-ceramic membranes, *e.g.* overcoming the permeability requirements for economically-competitive post-combustion CO_2 capture [1]. The molten salt (an alkali metal carbonate mixture) is typically supported in porous oxygen-ion and/or electron conducting solids [2–7]. In such cases, it has been proposed that co- or counter-current transport of oxygen-ions and/or electrons in the solid phase occurs concurrently with the transport of carbonate-like ions through the molten carbonate [7,8]. Therefore, the triple-phase boundary length (molten salt-gas-solid support) likely impacts permeation rate [7,9]. Use of a nominally inert support, far less common in the literature [10,11], should force permeation to occur within the molten salt alone (*i.e.* the permeation rate is now related to a two-phase boundary, the molten salt-gas interfacial area). Therefore, permeation rates should increase with an increase in molten salt-gas interfacial areas and/or a reduction in molten carbonate thickness within the support. As

* Corresponding author.
E-mail addresses: m.kazakli2@newcastle.ac.uk (M. Kazakli), greg.mutch@newcastle.ac.uk (G.A. Mutch), getriantafy@chemeng.upatras.gr (G. Triantafyllou), amggil3@gmail.com (A.G. Gil), tao.li10@imperial.ac.uk (T. Li), bo.wang2@imperial.ac.uk (B. Wang), joshua.bailey@ucl.ac.uk (J.J. Bailey), d.brett@ucl.ac.uk (D.J.L. Brett), p.shearing@ucl.ac.uk (P.R. Shearing), kang.li@imperial.ac.uk (K. Li), ian.metcalfe@newcastle.ac.uk (I. Metcalfe).

https://doi.org/10.1016/j.memsci.2020.118640
Received 22 May 2020; Received in revised form 4 August 2020; Accepted 18 August 2020
Available online 21 August 2020
0376-7388/© 2020 The Authors. Published by Elsevier B.V. This is an open access article under the CC BY license (http://creativecommons.org/licenses/by/4.0/).

CO_2 has specific chemical interactions with molten carbonate, very high CO_2 selectivity should also be realised ($CO_2/N_2 > 1000$) [12]. However, CO_2 permeation in molten carbonates is complex, covered in detail elsewhere [7]. Briefly, it is likely that a facilitated transport mechanism exists, due to the presence of potential mobile carriers that have been shown to have reactivity with CO_2 (*e.g.* O^{2-} or CO_3^{2-}). Surface reactions facilitate adsorption of CO_2 in to, and desorption of CO_2 out of the melt, with bulk diffusion of mobile carrier complexes mediating transport through the membrane, by *e.g.* an oxo-Grotthuss mechanism [13]. Ultimately, an improved understanding of permeation in molten carbonate supported in a nominally inert material could eliminate the requirement for more expensive oxygen-ion and/or electron-conducting materials as supports.

To date, dual-phase membranes have made use of supports in pellet [2,10], hollow-fibre [14–16], and tubular geometries [17,18]. Molten carbonate thickness has been controlled in pellet and tubular geometries by employing asymmetric structures, where two solid phases with disparate molten carbonate wettabilities are employed. One solid is a highly-wettable thin layer for supporting molten carbonate and the other is a thick non-wettable layer for mechanical strength [6,17–19]. In these examples, fluxes were higher than those of comparable thicker membranes made of the highly-wettable material. Similar effects have been observed in tubular dual-phase membranes [18]. Even though a reduction in molten carbonate thickness leads to improved CO_2 fluxes, it has been noted that it is difficult to precisely define molten carbonate thickness within a porous support. Thickness is also of limited utility as it is the path length of the permeant that is important, which is difficult to determine in sinuous networks of pores (more common in membranes than *e.g.* linear pathways). Furthermore, such poorly-defined support geometries will likely lead to uncontrolled differences in interfacial areas or triple-phase boundary lengths, providing additional discrepancies when comparing fluxes. Often, precise interfacial areas are unknown and cannot be used directly. Therefore, it is typical to use a membrane surface area which approximates the dual-phase membrane structure as a smooth surface. However, this surface has different interfaces within it, and often characterisation is lacking. In the absence of precise measurements of interfacial areas, this leads to comparisons of membrane performance that are potentially misleading.

If we shift focus to supports for molten salts that are also realistically scalable, *i.e.* modular, one-step fabrication procedures, and with high membrane surface-area-to-volume ratios, asymmetric hollow-fibre supports are amongst the most suitable candidates [20]. However, the membrane surface area and/or interfacial area is very difficult to define precisely, as they are micro-tubular, with an asymmetric microstructure composed of at least two porosity domains: (i) micro-channels that are conically shaped with an open entrance on the inside surface (lumen), and (ii) a packed-pore network, located in-between the micro-channels and towards the outer surface (shell) (Fig. 1) [21]. Furthermore, a gradient in pore size exists in the packed-pore network, with larger pores at the lumen side and smaller pores at the shell side, culminating in a region referred to as the sponge-like layer (Fig. 1) [22]. To date, there have been very few studies on dual-phase hollow-fibre membranes (DPHFMs), and in all cases they were infiltrated with molten carbonate by immersing the hollow-fibre support in a "molten carbonate bath" [14–16]. Therefore, molten carbonate distribution was uncontrolled, spanned the entire support thickness and infiltrated both the packed-pore network and micro-channels. This conventional infiltration method produces membranes that are 'thicker', and with lower lumen-side molten salt-gas interfacial areas, than could be achieved by preparing DPHFMs without molten carbonate in the micro-channels. This potential for a reduction in thickness and/or an increase in molten salt-gas interfacial area has not been explored and could feasibly result in improved permeation rates [14].

Here, we aim to simplify the dual-phase membrane concept to better address fundamental questions related to permeation in molten salts by employing nominally inert Al_2O_3 supports. This should isolate CO_2 permeation to the molten salt alone and allow a more detailed understanding of *e.g.* the role of molten salt-gas interfacial area and the effect of molten salt thickness, all in the absence of support contributions. First, we fabricated model membranes where the diffusional path length in the molten salt was equal to the molten salt thickness, thus tortuosity of unity, and with well-defined molten salt-gas interfacial areas. The model membranes allowed us to determine temperature regions where surface-exchange and diffusion processes were likely rate-limiting. We then prepared mechanically robust and well-characterised Al_2O_3 hollow-fibre supports and employed a newly developed carbonate infiltration method which allowed us to control carbonate distribution. We show that an increase in permeate-side molten salt-gas interfacial area (as determined by X-ray micro-computed tomography (X-ray micro-CT)) results in an increase in CO_2 permeation rate when operating in the surface-exchange rate-limited region. Overall, through model membrane experiments, a new molten carbonate infiltration method and robust mechanical and physical characterisation, we demonstrate that improved permeation rates can be achieved by carefully controlling molten carbonate distribution (*viz.* molten salt-gas interfacial area and/or diffusional path length) within dual-phase molten salt-ceramic membranes.

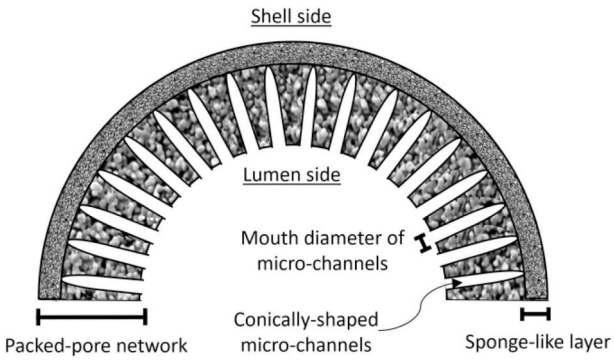

Fig. 1. Porosity domains of a micro-structured hollow-fibre support. Schematic representation of a hollow-fibre cross-section showing the conically shaped micro-channels and the mouth diameter of the conically shaped micro-channels, as well as the packed-pore network and its sponge-like layer.

2. Experimental

2.1. Preparation of model Al_2O_3 crucible membrane supports

Dense Al_2O_3 cylindrical crucibles (1.4 cm H, 2.55 cm OD, 2.2 cm ID) (Almath), with a base of 440 μm thickness, were used as the supports for the preparation of model dual-phase crucible membranes. The crucibles were laser-drilled by Laser Micromachining Limited, from the external base of the crucible towards the internal surface forming truncated cone-shaped pores within a central 11 mm diameter. The larger diameter of the truncated cone was on the external surface of the crucibles. Optical microscopy was used to determine the geometrical properties of the drilled surface of the Al_2O_3 crucibles.

2.2. Preparation of asymmetric Al_2O_3 hollow-fibre supports

Asymmetric Al_2O_3 hollow-fibre supports were prepared by a viscous-fingering-induced phase-inversion and sintering technique [20,21,23,24]. The ceramic suspension for their preparation consisted of α-Al_2O_3 powder, dimethyl sulfoxide (VWR) as the solvent, 0.4 wt% Arlacel P135 (Uniqema) as the dispersant and 6.3 wt% polyethersulfone (Ameco Performance) as the polymer binder. For the fabrication of asymmetric Al_2O_3 micro-structured hollow fibres, an Al_2O_3 suspension with 60 wt% solid loading was prepared by ball milling the above mixture. After degassing the ceramic suspension under vacuum to remove air bubbles,

it was then transferred into 200 ml stainless syringes and extruded through a tube-in-orifice spinneret (3 mm OD, 1.2 mm ID) at a rate of 7 ml min^{-1} into a coagulation bath of deionized water with no air gap (0 cm). The formed precursor fibres were submerged in deionized water for a minimum of 12 h to ensure the full removal of excess solvent. The precursor fibres were then gently washed with deionized water, straightened and dried at room temperature before sintering in a tubular furnace at either 1200, 1250, 1300 or 1350 °C in air [25]. Fibres were first heated to 600 °C at 2 °C min^{-1} before dwelling for 2 h to remove residual solvent. Subsequently they were heated to the final sintering temperature at 5 °C min^{-1} before dwelling for 4 h. Finally, they were cooled to room temperature at 3 °C min^{-1}. Porosity and pore size distribution was analysed by mercury intrusion porosimetry (MIP) (detailed in Supporting Data).

2.3. Preparation of eutectic carbonate mixture

To prepare the carbonate mixture, solid-state Li_2CO_3 (99%, Alfa Aesar), Na_2CO_3 (99.5%, Alfa Aesar), and K_2CO_3 (99%, Alfa Aesar) were placed in individual crucibles and dried in a furnace at 400 °C for 24 h. The dried carbonates were then mixed in a eutectic molar ratio (Li_2CO_3: Na_2CO_3: K_2CO_3 = 43.5: 31.5: 25.0) and the mixture was dispersed in ethanol to a concentration of 0.025 g l^{-1}. To reduce the average particle size and narrow the particle size distribution, the suspension was placed in a ball miller (Pascall Engineering, Parvalux electric motor) for a period of 48 h at 30 rpm with 15 YSZ milling balls of 1 cm diameter. The particle size and particle size distribution of the carbonates were measured at specific time intervals during the milling and after 48 h using dynamic light scattering with non-invasive backscatter optics (Malvern Panalytical, Zetasizer Nano ZS).

2.4. Infiltration of dual-phase Al_2O_3 hollow-fibre membranes

DPHFMs were prepared by a novel two-step coating method. The fibres were first glazed on both sides with a commercial ceramic sealant (Scarva, G261/W) (diluted in deionized water), with 4 cm in the middle uncovered as the active membrane length, in order to match the isothermal zone of the furnace used for the permeation experiments. The Al_2O_3 hollow fibres were dip-coated in the glazing solution, and left to dry for 1 h. The tips of the hollow fibres were also glazed, in order to create a dead-end configuration. The glazed part of the fibre was gas-tight (confirmed by a pressure-drop method, Section 2.5) and did not contribute to the permeation measurements. During the next step, the partially-glazed fibres were coated with the solid carbonate layer on their outer surface by a vacuum-assisted method as shown in Fig. S1. The volume of mercury intruding in the support's porosity during the MIP tests was used to calculate the required quantity of carbonates to infiltrate: (i) the packed-pore network only for DPHFMs with a controlled distribution of carbonates and, (ii) the packed-pore network and micro-channels to simulate a conventionally prepared DPHFM. The density used for the above calculations was the density of the eutectic carbonate mixture at room temperature, $\rho = 2.36$ g cm^{-3}. Before coating the glazed fibres with the carbonate layer, they were then attached to a flexible rubber tube and a vacuum pump (Welch, 2027 Vacuum System) and immersed in the carbonate suspension. By applying a vaccum on the open-end of the fibres, ethanol was retained in the solvent trap and a carbonate layer was formed on the outer surface of the hollow fibre. The carbonate suspension was stirred throughout the coating process, using a magnetic stirrer (1000 rpm), aiming to achieve a homogeneous carbonate layer on the outer surface of the hollow fibres (Fig. S1b). The carbonate coating was compacted under vacuum for 10 min after the coated fibre was removed from the suspension. The residual solvent was evaporated at 50 °C in a drying oven for 5 h.

The infiltrated Al_2O_3 hollow fibres used for gas-tightness measurements at room temperature were heated to 600 °C at 1 °C min^{-1} before dwelling for 1 h in order to infiltrate the carbonate mixture into the porous support. The samples were then cooled down to room temperature, using the same rate, and the infiltrated hollow fibres were immediately stored in a desiccator (the carbonate mixture is highly hygroscopic). The loading of carbonates was determined by comparing the weight of the hollow fibres before and after the infiltration step. The DPHFMs used for CO_2 permeation measurements were infiltrated *in-situ* during each experiment (Section 2.5). The microstructure of the prepared DPHFMs were analysed by scanning electron microscopy (SEM), energy dispersive X-ray spectroscopy (EDX) and X-ray micro-CT (detailed in Supporting Data).

2.5. CO_2 permeation experiments

To prepare the permeation apparatus, a DPHFM was inserted into a custom-made reactor with a stainless-steel base and a quartz shell, as shown in Fig. 2. The quartz part of the apparatus was then placed and centered inside a tubular vertical furnace so that the active membrane length of the carbonate-coated Al_2O_3 hollow fibre (1) was aligned with the furnace's isothermal zone and the sealants (3 and 6) were kept outside the heating zone of the furnace. The feed and permeate gases were confined in two different chambers: one on the lumen side of the DPHFM and the other on the outer surface of the DPHFM. In order to achieve the creation of two isolated chambers the fibre was sealed with vacuum grease (3) at the base of the permeation apparatus which remained outside the heating zone of the furnace.

The flow rates of gases were controlled by individual mass flow controllers (Bronkhorst, EL-FlOW® Select) attached to a collective reader (Bronkhorst, HIGH-TECH®). The permeate-side sweep gas (4) was introduced into the permeation apparatus *via* a stainless-steel needle (5) (STN, 19G). The temperature of the vertical furnace (Carbolite®, EVA/EVC) was controlled by a temperature controller (Eurotherm, 3216 PID) and monitored by a type-K thermocouple (8) located near the outer surface of the membrane. The composition of the permeate side gas was analysed in-line first by an infrared analyser (Vaisala, CARBOCAP® CO_2 Probe GMP343) and then by a quadrupole mass spectrometer (ESS, GeneSys). The permeation performance of the DPHFMs was evaluated at 600 °C (nominal P = 1 atm in both chambers), and each experimental gas condition, after 1 h of stabilisation time, with a routine flux deviation of less than 3%. The total gas flow rate of each stream was monitored with an electronic flow meter (ThermoFisher Scientific, GFM Pro).

Before the sweep and feed gases were introduced, the system was purged with Ar (50 ml min^{-1}) for 10 min and checked for leaks. In the absence of leaks, the DPHFM was heated to the desired temperature to infiltrate the hollow fibre with molten carbonate and begin permeation experiments. The melting of the eutectic carbonate mixture typically occurred between 400 and 430 °C under a CO_2 partial pressure (pCO_2) of 0.5 atm in N_2. The feed gases used for the permeation experiments contained a pCO_2 of 0.1, 0.5, and 0.9 atm in N_2, whereas the pCO_2 in the sweep gases used were: 0, 0.0004 and 0.01 atm in Ar. All permeation experiments were conducted at atmospheric pressure.

For the model dual-phase crucible membranes, a similar dual chamber set-up as described above for the DPHFMs was used [26]. The crucibles were mounted on top of a hollow Al_2O_3 tube using a high-temperature sealant (Fuel Cell Materials, Silver, AG-1) and left to dry in a drying oven at 100 °C for a minimum of 12 h. The eutectic carbonate mixture was added in different amounts (0.2, 0.4, 0.6 and 0.8 g) into the crucible, in separate experiments, to produce membranes with well-defined permeation path lengths. The amount of carbonates needed to deposit carbonate layers with 250, 500, 750, 1000 μm thickness on top of the Al_2O_3 crucibles was calculated by converting the volume corresponding to the desired membrane thickness to the equivalent amount of carbonates. The volume expansion of carbonates was also taken into consideration and all the calculations were made for a volume increase of 15% between ambient temperature and 500 °C. The pCO_2 in N_2 used in the feed gas was 0.5 atm (50 ml min^{-1}) and Ar was used as the sweep gas (50 ml min^{-1}), with the base of the crucible as

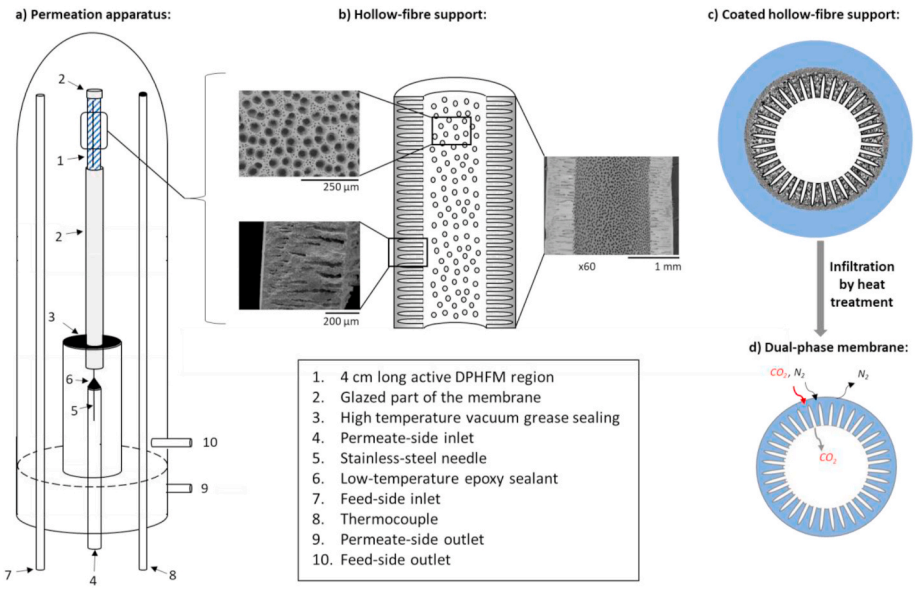

Fig. 2. Permeation apparatus and DPHFM structure. a) Permeation apparatus, b) an Al_2O_3 hollow-fibre support and three SEM micrographs of its microstructure, c) Coated Al_2O_3 hollow-fibre support at room temperature and d) Permeation mechanism of a dual-phase membrane after infiltration of carbonates by heat treatment.

the permeate side and the reservoir of molten carbonate in the crucible as the feed side.

The permeate-side flux of the dual-phase membranes was evaluated between 500 and 800 °C and the composition of the permeate gas was analysed first by an infrared analyser (Emerson, Rosemount X-STREAM X2GP) and then by an in-line quadrupole mass spectrometer (Hiden, QGA). The calibration curve for each gas, was obtained by a three-point calibration of both the mass spectrometer and the IR analyser, in line. To calibrate the zero background, high-purity Ar was used. Calibrations for drift of the analytical equipment were performed at the operating membrane temperature, 600 °C, during experiments. Volumetric flux, J_{CO2} (ml min^{-1} cm^{-2}), of CO_2 through the membranes was calculated using Eq. (1):

$$J_{CO_2} = \frac{x_{CO_2}\,\dot{V}}{A_S} \qquad \text{(Eq. 1)}$$

where x_{CO_2} is the mole fraction of CO_2 in the permeate-side outlet, V is the volumetric flow rate on the permeate side (ml min^{-1}) and A_S is the membrane interfacial area (cm^2). Detail on the definition and measurement of membrane interfacial area is provided below. To quantify and subtract N_2 leakage through the membrane, the following procedure was adopted (after subtracting the zero background for both gases). First, if the permeate-side N_2 flux was equal to or greater than that of CO_2, membrane sealing was considered unsuccessful and the experiment was terminated. In the experiments presented in this work N_2 leakage was extremely low, at or around the calibrated zero value for N_2 gas (in

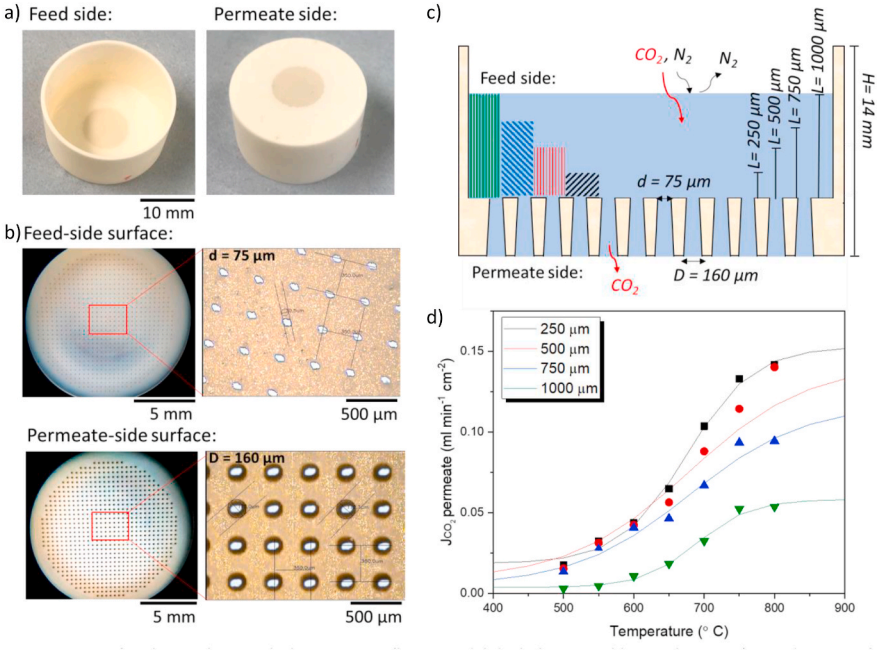

Fig. 3. Impact of molten carbonate thickness on CO_2 flux in model dual-phase crucible membranes. a) Digital images of model dual-phase crucible membranes with laser-drilled pores, b) feed- and permeate-side surfaces with pore dimensions, c) cross-section of drilled crucibles with different molten carbonate thicknesses achieved by filling the crucibles with different amounts of molten carbonate (note: membrane thickness is therefore the thickness of the carbonate layer plus the thickness of the pores (440 µm)) and, d) effect of molten carbonate thickness and temperature on CO_2 flux where experimentally determined data points were fitted using a sigmoidal function (note: temperature was initially increased at 1 °C min^{-1} to 800 °C before dwelling for 7 h, with subsequent decreases at 1 °C min^{-1} to 750, 700, 650, 600, 550 and 500 °C with 7 h dwells at each temperature).

all cases this translated to a N_2 flux < 0.01 ml min^{-1} cm^{-2}). However, to correct CO_2 flux such small leakages of N_2 were subtracted from the CO_2 flux.

3. Results and discussion

3.1. Permeation performance of dense Al_2O_3 laser-drilled model membranes

To investigate the effect of molten carbonate thickness, molten salt-gas interfacial area and temperature on CO_2 flux, model dual-phase crucible membranes were fabricated (Fig. 3a). The model crucible membranes employed a nominally inert and dense Al_2O_3 support, so that permeation was isolated to the molten carbonate phase. The pores created by laser-drilling the 440-μm-thick base of the Al_2O_3 crucibles had the shape of a truncated cone, with $D = 160$ μm and $d = 75$ μm, where D is the larger diameter (external base) and d is the smaller diameter (internal surface) (Fig. 3b). A total of 745 pores were drilled, providing a model membrane with a feed-side molten salt-gas interfacial area of 3.8 cm^2 (the molten carbonate surface in the 2.2 cm internal diameter crucible) and a permeate-side molten salt-gas interfacial area of 0.15 cm^2 (the sum of the areas of the truncated cone ends on the permeate-side) (Fig. 3b). First, by swapping the feed-side and permeate-side inlet streams, it was determined that the CO_2 permeation rate was proportional to the molten salt-gas interfacial area on the permeate side (*i.e.* desorption). As desorption was suspected to be the rate-determining step the permeate side interfacial area is used to calculate fluxes hereafter. Subsequently, the crucibles were filled with different amounts of carbonate, to produce membranes with well-defined carbonate thicknesses of 250, 500, 750 and 1000 μm on top of the drilled pores of 440 μm thickness (giving total membrane thicknesses of 690, 990, 1190 and 1440 μm) (Fig. 3c). In this arrangement, the permeate-side molten salt-gas interfacial area is well-defined and constant (0.15 cm^2) allowing direct comparisons of flux without the concern of uncontrolled differences in, or definitions of, membrane surface area when comparing different studies. A reduced molten carbonate thickness resulted in increased CO_2 flux at all temperatures (Fig. 3d). Fluxes increased with increasing temperature until 750 °C where a further increase in temperature did not result in significantly increased flux for all thicknesses. The experimentally determined fluxes were fitted through nonlinear regression to a sigmoidal function:

$$J_{CO_2} = \frac{J_{CO_2\_min} - J_{CO_2\_max}}{1 + e^{((T-T_{50})/dT)}} + J_{CO_2\_max} \quad \text{(Eq. 3)}$$

where J_{CO2_min} and J_{CO2_max} are the lowest and highest fluxes in the temperature range studied, T_{50} is the temperature at 50% of the highest flux measured, dT is a characteristic width of the linear section of the increase in flux and T is the temperature. Parameters J_{CO2_min}, J_{CO2_maX}, T_{50} and dT were initially identified by fitting the model to the data using a nonlinear solver. Regression coefficients (R^2) showed that the sigmoidal function fitted the data well ($R^2 > 0.97$). The model parameters were then adjusted according to the appropriate linear or polynomial fit obtained by plotting each parameter against the molten carbonate thickness for the 690, 990 and 1440 μm membranes. The model parameters for the membrane with 1190 μm of molten carbonate were interpolated in order to correct for the anomalous data point for this membrane at 800 °C. The results suggested that CO_2 flux through molten carbonate could be considered in two main temperature regions (Fig. 3d). Firstly, there is a low-temperature region (~500–750 °C) where flux increases significantly with temperature regardless of thickness. Here, there is likely a rate-limiting effect due to a surface-exchange process, as surface exchange is more strongly activated than diffusion. Based on the results of the first experiment, where we swapped feed-side and permeate-side inlet streams, it is likely that this rate-limiting surface-exchange process is at the permeate side. Secondly, there is a high-temperature region (>750 °C) where flux did not increase as significantly with increased temperature for a given thickness, more noticeably for thicker membranes. This would be consistent with a diffusion limitation becoming dominant.

3.2. Properties of micro-structured Al_2O_3 hollow fibres

The results from the model dual-phase crucible membranes showed that in dual-phase molten salt-ceramic membranes with a nominally-inert support, a practical way to increase CO_2 permeation rate in the low-temperature region (500–750 °C), would be to increase the molten salt-gas interfacial area at the permeate side. If the aim is to exploit this in a geometry with potential for scale-up and application, supports with a hollow-fibre geometry should be considered. Hollow fibres are modular and have a high membrane surface area-to-volume ratio/low mass transfer resistances at the lumen side due to the micro-channels (100–1000 higher mass transfer rates than in traditional packed and plate column contactors) [27–31]. Therefore, the key challenge is to prepare DPHFMs without infiltrating the micro-channels with molten carbonate (as this should increase the molten salt-gas interfacial area) and to subsequently employ the lumen as the permeate side in operation.

To prepare such DPHFMs it was necessary to determine the pore volume associated with each porosity domain of Al_2O_3 hollow-fibre supports so that during molten carbonate infiltration the packed-pore network was infiltrated but the micro-channels remained empty. Pore size distribution, determined by MIP, showed two distinct pore size domains (Fig. S2a). The micro-channels were represented by a wider peak from 5 to 20 μm, and the packed-pore network by a sharper peak at ~0.2 μm, agreeing closely with previous studies on Al_2O_3 hollow fibres [24]. This difference in pore size is advantageous for our aims, as the higher capillarity in the pores of the packed-pore network should assist in restricting the molten carbonate to the packed-pore network. To determine the pore volume associated with the packed-pore network and therefore the quantity of carbonate required to fill the network, the normalised cumulative intrusion volume was used. The intruded volume at ~5000 kPa was subtracted from the intruded volume at the highest intrusion pressure of ~14000 kPa (Fig. S2b), to give pore volumes of 0.30, 0.29, 0.27 and 0.17 ml g^{-1} for the packed-pore network of hollow fibres sintered at 1200, 1250, 1300 and 1350 °C, respectively. Also observable in Fig. S2a and b, is the loss of pore volume with the increase in sintering temperature, which may negatively impact our goal of infiltrating the packed-pore network. However, increasing the sintering temperature also increased the mechanical strength of hollow fibres, which is important considering their fragile nature [5,9,10]. Therefore, to establish the best trade-off relationship between mechanical strength and porosity for the DPHFM supports, 3-point bending tests were performed on hollow fibres sintered at 1200, 1250, 1300, and 1350 °C (Fig. S2c). It was decided that hollow fibres sintered at 1300 °C offered the best trade-off between mechanical strength and porosity (Fig. S2c), and are therefore used exclusively in further experiments.

3.3. Controlling carbonate distribution in DPHFMs

3.3.1. Incorporation of carbonates

To limit the infiltration of carbonates to the packed-pore network of the hollow fibres, the quantity of solid carbonate powder required to occupy the packed-pore network (calculated using the MIP results) was deposited on the outer surface of the hollow fibres using a new vacuum-assisted method (Fig. S1a). As the average pore size of the packed-pore network on the outer surface of the hollow fibres was ~0.2 μm (Fig. S2a), the carbonate powder was prepared by ball-milling so that the average particle size of the carbonates was ~0.8 μm. In this way, the layer was deposited without penetrating the hollow fibre (Fig. 4a and b). Following heat treatment at 600 °C, the carbonate mixture infiltrated the hollow-fibre supports due to the capillarity of the pores and the good

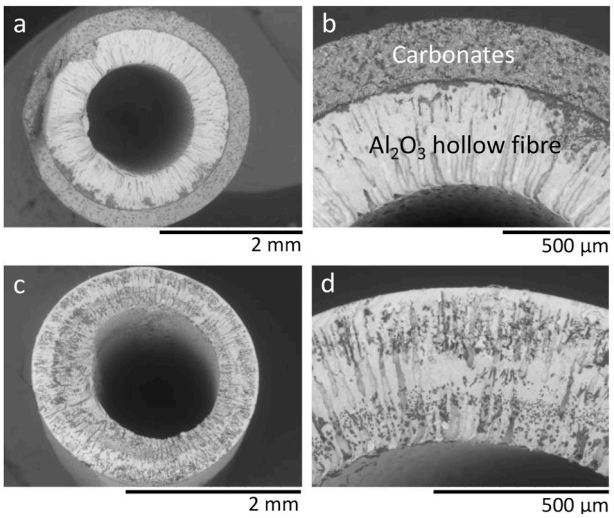

Fig. 4. Coating and controlled distribution of carbonates in Al_2O_3 hollow fibres. a) and, b) SEM images of an Al_2O_3 hollow fibre coated with a carbonate layer at room temperature by a vacuum-assisted method and, c) and, d) SEM images of an Al_2O_3 hollow fibre infiltrated with carbonates after heat treatment at 600 °C. Note that the micro-channels remain visible as they have not been significantly infiltrated with carbonates. Note also that the images are in a) and c) are from different sections of hollow fibres and therefore direct comparisons of e.g. inner diameter are not possible due to variations in thickness along the length of a single fibre.

wettability of molten carbonate on Al_2O_3 [11]. As the packed-pore network has a smaller average pore diameter (~0.2 µm) compared to the micro-channels (>10 µm), and therefore higher capillarity, the molten carbonate did not significantly penetrate the micro-channels (shown as a thin white layer of solidified carbonate at room temperature in Fig. 4c, with the micro-channels still clearly visible in Fig. 4c and d). Of course carbonates may migrate once molten, but due to the differences in capillarity and the high capillary force achieveable in such small pores [7], it is reasonable to suggest that the majority of the carbonates will remain in the packed-pore network during operation at ambient pressure. One further important difference compared to a conventional infiltration method, is that we now have a distribution in molten carbonate thickness, where the minimum is the thickness of the sponge-like layer (~50 µm), and the maximum is the hollow-fibre thickness (~500 µm).

3.4. Performance of DPHFMs in CO_2 separation

To investigate the impact of our new preparation method on separation performance, we also followed a conventional DPHFM preparation method, aiming to fabricate a DPHFM where the packed-pore network and micro-channels were both filled with molten-carbonate (Fig. S3). To elucidate the resulting membrane structure (Fig. 5), we investigated representative sections of the DPHFMs (~2–3 mm length) using X-ray micro-CT (Fig. 6a and b). Experiments were conducted at room temperature and as such the carbonates were in the solid state; the impact of the deviation from operating conditions is discussed below. 3D reconstructions of the X-ray data clearly showed significant structural differences between the preparation methods (Fig. 6a and b). A greater fraction of empty micro-channels were visible in the DPHFM prepared following our new method confirming that the method was successful in confining the majority of the molten salt to the packed-pore network. Note that the reconstructions in Fig. 6 were segmented during post-processing so that solids (Al_2O_3 and carbonates) were differentiated from porosity (Fig. S4). Porosity was further distinguished as connected and unconnected (to the lumen surface of the membrane). Segmenting the Al_2O_3 and solid carbonates as one phase allowed us to visualise the

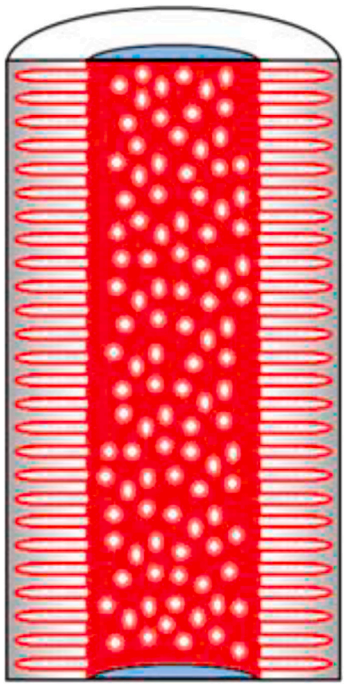

Fig. 5. Cross-sectioned interfacial area schematic. The permeate-side solid-gas interfacial area is shown in red. It is calculated by subtracting the surfaces shown in blue from the surface area of the connected pores. (For interpretation of the references to colour in this figure legend, the reader is referred to the Web version of this article.)

non-infiltrated micro-channels at the lumen side and determine a lumen-side solid-gas interfacial area. This interfacial area is defined as the area of contact between voxels segmented as solids and those segmented as connected porosity. In order to calculate this quantity, the blue shaded surface area in Fig. 5 was subtracted from the total surface area of the connected porosity, to yield only the interfacial area where connected porosity directly contacts the solids (red in Fig. 5) (*i.e.* Solid-gas interfacial area = connected porosity surface area (red) – cross-sectioned connected porosity surface area (blue lids)). This solid-gas interfacial area, shown in Table 1 normalised for hollow-fibre length, was increased from 2.07 cm^2/cm to 7.47 cm^2/cm following our new preparation method.

CO_2 permeation rates for both DPHFMs were measured at 600 °C so that we were operating within the permeate-side surface-exchange limited regime (Fig. 6c). Furthermore, we employed the lumen side as the permeate side to take advantage of the increased interfacial area resulting from our new preparation method (with non-infiltrated, open micro-channels). The effect of driving force was also studied by varying pCO_2 at the feed-side inlet (0.1, 0.5 or 0.9 atm CO_2 in N_2), and the permeate-side inlet (either pure Ar, or 0.0004 or 0.01 atm CO_2 in Ar). The permeation rates in Fig. 6c were extracted from permeation experiments routinely lasting >100 h. The single points in Fig. 6c were extracted by taking an average rate from at least a 1 h period at the end of the relevant experimental condition (Fig. S5). CO_2 permeation rates increased with an increased partial pressure difference driving force, both in the case of increasing the pCO_2 at the feed-side inlet, and in the case of decreasing the pCO_2 at the permeate-side inlet. At all driving forces studied the DPHFM prepared without infiltrating the micro-channels provided higher permeation rates, demonstrating the advantage of the preparation method under a wide variety of conditions. For example, at the highest driving force studied the permeation rate was increased ~4-fold (Fig. 6c) for a ~3.6-fold increase in solid-gas interfacial area (Table 1). This increase in solid-gas interfacial area (2.07 cm^2/cm to 7.47 cm^2/cm) was determined by X-ray micro-CT measurements where the Al_2O_3 support and carbonates were segmented as one

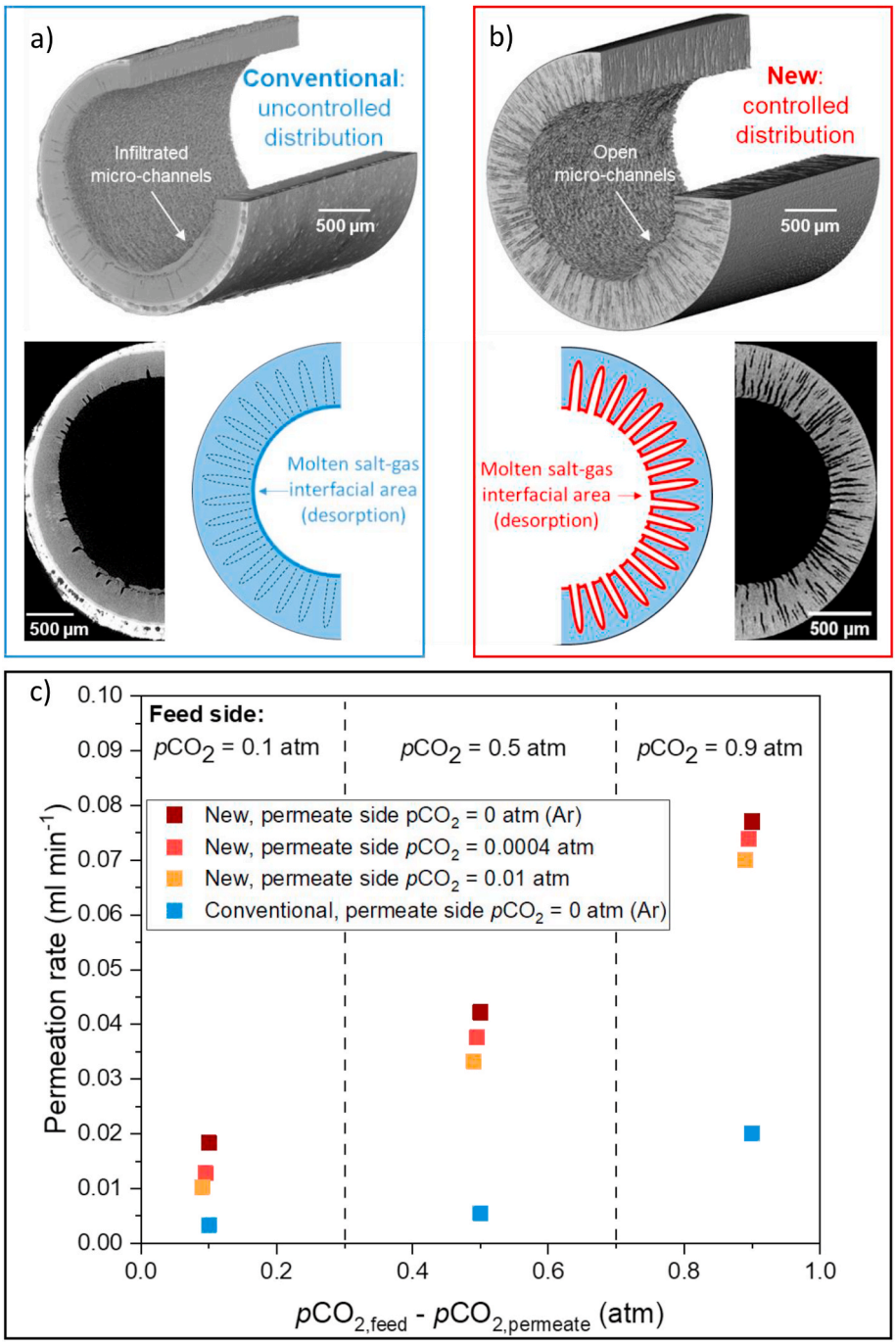

Fig. 6. DPHFMs performance. a) X-ray micro-CT reconstruction of a conventionally prepared DPHFM and, b) following our controlled preparation method. c) The effect of preparation method and driving force on the CO_2 permeation rate through DPHFMs at 600 °C. Note also that the conventionally prepared DPHFM used a thinner hollow-fibre support (~250 µm compared to ~500 µm, Fig. S4) further emphasising the positive effect of increased interfacial area.

solid phase. Of course, the carbonates would be molten in operation and therefore the wetting and mobility of carbonates in the molten state is not accounted for. In addition, moving from the solid to molten state, carbonate volume increases. Finally, the nominally electronically insulating Al_2O_3 support likely does not contribute to permeation and under different driving forces, different pores may contribute to permeation. Thus, the reported solid-gas interfacial values approximate multiple competing effects that would become apparent in operation. First, molten carbonate may be retained within the packed-pore network due to capillary forces, which would reduce the 'active' interfacial area to a fraction of the gas-solid interfacial area determined here. This would be dependent on the surface porosity of the micro-channels which is difficult to determine with high precision due to their microstructure and gradient in pore size within them. Alternatively, considering the good wettability of molten carbonate on Al_2O_3, the entire Al_2O_3 surface may be wetted by a thin layer of molten carbonate rendering our results reasonably precise (*i.e.* the entire solids surface area in Table 1 is wetted with carbonate). As a final point, it is possible that *e.g.* $LiAlO_2$ forms at the interface between Al_2O_3 and the molten carbonates. It is unlikely that this significantly impacted the interpretation of permeation results as (i) the quantity of CO_2 released from the permeate side over the course of a typical permeation experiment was well above that which would come from full conversion of Al_2O_3 to $LiAlO_2$ and (ii) the permeation experiments provided stable permeation rates for up to 10^2

Table 1
DPHFM interfacial areas extracted from X-ray micro-CT segmented datasets. Total solids is defined as the ceramic hollow fibre and solid carbonates combined (as the analysis was at room temperature, the carbonates were in the solid state). Connected or unconnected porosity refers to void space in the support and whether it is connected to the lumen side. The fraction of the total analysed volume associated with each is given. Surface areas of the components shown in Fig. 5 are given normalised for hollow-fibre length and can be inter-related using the equation: total solids surface area = feed-side surface area (outer curved surface area of cylinder) + cross-sectioned solid surface area (white rings) + unconnected porosity area (not shown in figure) + connected porosity area (red surface and blue lids) – cross-sectioned connected porosity area (blue lids).

Preparation Method	Total solids (Al_2O_3 and carbonates)		Feed-side (outer curved surface area of cylinder)	Cross-sectioned solid surface area (white rings)	Unconnceted porosity (not shown in figure)		Connected porosity (red surface and blue lids)		Cross-sectioned connected porosity area (blue lids)	Solid-gas interfacial area
	Surface Area (cm^2/cm)	Fraction (%)	Surface Area (cm^2/cm)	Surface Area (cm^2)	Surface Area (cm^2/cm)	Fraction (%)	Surface Area (cm^2/cm)	Fraction (%)	Surface Area (cm^2)	(cm^2/cm)
New	10.42	54.9	0.85	0.06	2.04	1.2	7.51	43.9	0.04	7.47
Conventional	3.55	38.8	1.08	0.04	0.37	0.4	2.13	60.7	0.06	2.07

h. It is likely that we did not observe this reaction in our experiments as any small release of CO_2 due to it was obscured by the high background of CO_2 on both sides of the membrane during initial heating. Overall, the structural analysis clearly confirms that an increase in the permeate-side interfacial area (be it solid-gas or molten salt-gas interfacial area) correlates well with an increase in permeation rate. Although this was measured here as a solid (Al_2O_3 and solid carbonate)-gas interfacial area it is important to recall that the Al_2O_3 support is inert, and therefore an increase in permeation rate is likely due to an increase in molten-salt gas interfacial area under operating conditions. In essence, we have shown that with two similar porous solids, where one has a wetted surface layer and the other has its porosity (the micro-channels in this case) entirely infiltrated with the same liquid phase, the latter will have a lower gas-liquid interfacial area and thus gives poorer performance in applications that rely on high interfacial areas such as membrane permeation.

4. Conclusions

Molten carbonate was supported in nominally inert Al_2O_3 to produce dual-phase molten salt-ceramic membranes where permeation was restricted to the molten salt alone. Model crucible membranes with controllable molten carbonate thickness and feed-/permeate-side molten salt-gas interfacial areas were fabricated and demonstrated a permeate-side, surface-exchange rate limiting effect during carbon dioxide permeation experiments at 500–750 °C. We exploited this effect in a realistically scalable support geometry, an asymmetric hollow fibre, by developing a new carbonate infiltration procedure to provide higher permeate-side interfacial areas. The ~3.6-fold increase in interfacial area relative to a conventional preparation procedure was determined by X-ray micro-CT and was correlated with up to a ~4-fold increase in permeation rate. Thus, our results demonstrate that careful control of carbonate distribution in hollow fibres can lead to improved efficiency of a DPHFM. We suggest that the adoption of more rigorous measurements of molten salt-gas interfacial areas or molten salt thickness (and in the case of conductive supports, triple-phase boundary lengths) would make literature data more robust and more easily comparable.

Author statement

All authors approve of submission to *Journal of Membrane Science*, we have no conflicts of interest to disclose, no competing interests to declare and confirm that the manuscript is not under consideration for publication elsewhere.

On behalf of all authors I thank you for your consideration and we look forward to hearing from you.

Declaration of competing interest

The authors declare that they have no known competing financial interests or personal relationships that could have appeared to influence the work reported in this paper.

Acknowledgments

The authors wish to thank Dr Oliver B. Camus at Bath University for conducting MIP measurements. The research leading to these results has received funding from the European Research Council under the European's Union Seventh Framework Programme (FP/2007-2013) / ERC Grant Agreement Number 320725 and from the Engineering & Physical Sciences Research Council (EPSRC) via grants EP/M01486X/1, EP/P007767/1 and EP/P009050/1. GAM was supported by the Royal Academy of Engineering under the Research Fellowship scheme and would like to thank the EPSRC for a Doctoral Prize Fellowship (EP/M50791X/1) and Newcastle University for support via a Newcastle University Academic Track (NUAcT) Fellowship. X-Ray access was supported by UCL and EPSRC under EP/N032888/1. PRS acknowledges The Royal Academy of Engineering (CiET1718/59). JJB, DJLB, PRS acknowledge The Faraday Institution Nextrode Programme (EP/S003053/1, FIRG015). Data supporting this publication is available under a Creative Commons Attribution 4.0 International license, see DOI: 10.25405/data.ncl.9609200.

Appendix A. Supplementary data

Supplementary data related to this article can be found at https://doi.org/10.1016/j.memsci.2020.118640.

References

[1] L. McNeil, G.A. Mutch, F. Iacoviello, J. Bailey, G. Triantafyllou, D. Neagu, T. Miller, E.I. Papaioannou, W. Hu, D. Brett, P. Shearing, I.S. Metcalfe, Dendritic silver self-assembly in molten-carbonate membranes for efficient carbon dioxide capture, Energy Environ. Sci. 13 (2020) 1766–1775.
[2] M. Anderson, Y.S. Lin, Carbonate–ceramic dual-phase membrane for carbon dioxide separation, J. Membr. Sci. 357 (2010) 122–129, https://doi.org/10.1016/j.memsci.2010.04.009.
[3] S.J. Chung, J.H. Park, D. Li, J.-I. Ida, I. Kumakiri, J.Y.S. Lin, Dual-phase Metal−Carbonate membrane for high-temperature carbon dioxide separation, Ind. Eng. Chem. Res. 44 (2005) 7999–8006, https://doi.org/10.1021/ie0503141.
[4] Z. Rui, M. Anderson, Y. Li, Y.S. Lin, Ionic conducting ceramic and carbonate dual phase membranes for carbon dioxide separation, J. Membr. Sci. (2012) 174–182, https://doi.org/10.1016/j.memsci.2012.06.030, 417–418.
[5] J. Sunarso, S. Baumann, J.M. Serra, W.A. Meulenberg, S. Liu, Y.S. Lin, J.C.D. da Costa, Mixed ionic–electronic conducting (MIEC) ceramic-based membranes for oxygen separation, J. Membr. Sci. 320 (2008) 13–41, https://doi.org/10.1016/j.memsci.2008.03.074.
[6] B. Lu, Y.S. Lin, Synthesis and characterization of thin ceramic-carbonate dual-phase membranes for carbon dioxide separation, J. Membr. Sci. 444 (2013) 402–411, https://doi.org/10.1016/j.memsci.2013.05.046.
[7] G.A. Mutch, L. Qu, G. Triantafyllou, W. Xing, M.-L. Fontaine, I.S. Metcalfe, Supported molten-salt membranes for carbon dioxide permeation, J. Mater. Chem. A. 7 (2019) 12951–12973, https://doi.org/10.1039/c9ta01979k.

[8] Z. Rui, M. Anderson, Y.S. Lin, Y. Li, Modeling and analysis of carbon dioxide permeation through ceramic-carbonate dual-phase membranes, J. Membr. Sci. 345 (2009) 110–118, https://doi.org/10.1016/j.memsci.2009.08.034.
[9] J. Fang, J. Tong, K. Huang, A superior mixed electron and carbonate-ion conducting metal- carbonate composite membrane for advanced fl ue-gas carbon capture, J. Membr. Sci. 505 (2016) 225–230, https://doi.org/10.1016/j.memsci.2016.01.041.
[10] J.L. Wade, C. Lee, A.C. West, K.S. Lackner, Composite electrolyte membranes for high temperature CO_2 separation, J. Membr. Sci. 369 (2011) 20–29, https://doi.org/10.1016/j.memsci.2010.10.053.
[11] M. Kazakli, G.A. Mutch, L. Qu, G. Triantafyllou, I.S. Metcalfe, Autonomous and intrinsic self-healing Al_2O_3 membrane employing highly-wetting and CO_2-selective molten salts, J. Membr. Sci. 600 (2020) 117855, https://doi.org/10.1016/j.memsci.2020.117855.
[12] M.R. Cerón, L.S. Lai, A. Amiri, M. Monte, S. Katta, J.C. Kelly, M.A. Worsley, M. D. Merrill, S. Kim, P.G. Campbell, Surpassing the conventional limitations of CO_2 separation membranes with hydroxide/ceramic dual-phase membranes, J. Membr. Sci. 567 (2018) 191–198, https://doi.org/10.1016/j.memsci.2018.09.028.
[13] D. Corradini, F. Coudert, R. Vuilleumier, Carbon dioxide transport in molten calcium carbonate occurs through an oxo-Grotthuss mechanism via a pyrocarbonate anion, Nat. Chem. 8 (2016) 454–460, https://doi.org/10.1038/nchem.2450.
[14] M. Zuo, S. Zhuang, X. Tan, B. Meng, N. Yang, S. Liu, Ionic conducting ceramic-carbonate dual phase hollow fibre membranes for high temperature carbon dioxide separation, J. Membr. Sci. 458 (2014) 58–65, https://doi.org/10.1016/j.memsci.2014.01.047.
[15] S. Zhuang, Y. Li, M. Zuo, X. Tan, B. Meng, N. Yang, S. Liu, Dense composite electrolyte hollow fibre membranes for high temperature CO_2 separation, Separ. Purif. Technol. 132 (2014) 712–718, https://doi.org/10.1016/j.seppur.2014.06.025.
[16] X. Jiang, J. Zhu, Z. Liu, S. Guo, W. Jin, CO_2-Tolerant $SrFe_{0.8}Nb_{0.2}O_{3-\delta}$–carbonate dual-phase multichannel hollow fiber membrane for CO_2 capture, Ind. Eng. Chem. Res. 55 (2015) 3300–3307, https://doi.org/10.1021/acs.iecr.5b03036.
[17] X. Dong, J. Ortiz Landeros, Y.S. Lin, An asymmetric tubular ceramic-carbonate dual phase membrane for high temperature CO_2 separation, Chem. Commun. 49 (2013) 9654–9656, https://doi.org/10.1039/c3cc45949g.
[18] X. Dong, H.-C. Wu, Y.S. Lin, CO_2 permeation through asymmetric thin tubular ceramic-carbonate dual-phase membranes, J. Membr. Sci. 564 (2018) 73–81, https://doi.org/10.1016/j.memsci.2018.07.012.
[19] B. Lu, Y.S. Lin, Asymmetric thin samarium doped cerium oxide-carbonate dual-phase membrane for carbon dioxide separation, Ind. Eng. Chem. Res. 53 (2014) 13459–13466, https://doi.org/10.1021/ie502094j.
[20] B.F.K. Kingsbury, K. Li, A morphological study of ceramic hollow fibre membranes, J. Membr. Sci. 328 (2009) 134–140, https://doi.org/10.1016/j.memsci.2008.11.050.
[21] A. Gouveia Gil, Z. Wu, D. Chadwick, K. Li, Microstructured catalytic hollow fiber reactor for methane steam reforming, Ind. Eng. Chem. Res. 54 (2015) 5563–5571, https://doi.org/10.1021/ie504953j.
[22] A.G. Gil, Z. Wu, D. Chadwick, K. Li, A catalytic hollow fibre membrane reactor for combined steam methane reforming and water gas shift reaction, Chem. Eng. Sci. 137 (2015) 364–372, https://doi.org/10.1016/j.ces.2015.06.051.
[23] B.F.K. Kingsbury, Z. Wu, K. Li, A morphological study of ceramic hollow fibre membranes: a perspective on multifunctional catalytic membrane reactors, Catal. Today 156 (2010) 306–315, https://doi.org/10.1016/j.cattod.2010.02.039.
[24] M. Lee, Z. Wu, R. Wang, K. Li, Micro-structured alumina hollow fibre membranes – potential applications in wastewater treatment, J. Membr. Sci. 461 (2014) 39–48, https://doi.org/10.1016/j.memsci.2014.02.044.
[25] A.G. Gil, M.H.M. Reis, D. Chadwick, Z. Wu, K. Li, A highly permeable hollow fibre substrate for Pd/Al_2O_3 composite membranes in hydrogen permeation, Int. J. Hydrogen Energy 40 (2015) 3249–3258, https://doi.org/10.1016/j.ijhydene.2015.01.021.
[26] S.G. Patrício, E.I. Papaioannou, B.M. Ray, I.S. Metcalfe, F.M.B. Marques, Composite CO_2 separation membranes: insights on kinetics and stability, J. Membr. Sci. 541 (2017) 253–261, https://doi.org/10.1016/j.memsci.2017.07.008.
[27] A.J. Brown, N.A. Brunelli, K. Eum, F. Rashidi, J.R. Johnson, W.J. Koros, C. W. Jones, S. Nair, Interfacial microfluidic processing of metal-organic framework hollow fiber membranes, Science 345 (2014) 72–75, https://doi.org/10.1126/science.1251181.
[28] W.J. Koros, C. Zhang, Materials for next-generation molecularly selective synthetic membranes, Nat. Mater. 16 (2017) 289.
[29] N. Bhuwania, Y. Labreche, C.S.K. Achoundong, J. Baltazar, S.K. Burgess, S. Karwa, L. Xu, C.L. Henderson, P.J. Williams, W.J. Koros, Engineering substructure morphology of asymmetric carbon molecular sieve hollow fiber membranes, Carbon N. Y. 76 (2014) 417–434, https://doi.org/10.1016/j.carbon.2014.05.008.
[30] L.-Z. Zhang, Heat and mass transfer in a randomly packed hollow fiber membrane module: a fractal model approach, Int. J. Heat Mass Tran. 54 (2011) 2921–2931, https://doi.org/10.1016/j.ijheatmasstransfer.2011.03.005.
[31] I. Voigt, H. Richter, M. Stahn, M. Weyd, P. Puhlfürß, V. Prehn, C. Günther, Scale-up of ceramic nanofiltration membranes to meet large scale applications, Separ. Purif. Technol. 215 (2019) 329–334, https://doi.org/10.1016/j.seppur.2019.01.023.